Biomimetic flow control

Biomimetic spiroid winglets for lift and drag control

Joel E. Guerrero *, Dario Maestro, Alessandro Bottaro

University of Genoa, Department of Civil, Environmental and Architectural Engineering, DICAT, Via Montallegro 1, 16145 Genoa, Italy

A R T I C L E   I N F O

A B S T R A C T

In aeronautical engineering, drag reduction constitutes a challenge and there is room for improvement and innovative developments. The drag breakdown of a typical transport aircraft shows that the lift-induced drag can amount to as much as 40% of the total drag at cruise conditions and 80–90% of the total drag in take-off configuration. One way of reducing lift-induced drag is by using wingtip devices. By applying biomimetic abstraction of the principle behind a bird's wingtip feathers, we study spiroid wingtips, which look like an extended blended wingtip that bends upward by 360 degrees to form a large rigid ribbon. The numerical investigation of such a wingtip device is described and preliminary indications of its aerodynamic performance are provided.

1. Introduction

From an aerodynamicist's point of view, the main motivation behind all wingtip devices is to reduce lift-induced drag. Recently, aircraft manufacturers are under increasing pressure to improve efficiency due to rising operating costs and environmental issues, and this has led to some innovative developments for reducing lift-induced drag. Several different types of wingtip devices have been developed during this quest for efficiency and the selection of the wingtip device depends on the specific situation and the airplane type. In Fig. 1, some of the wingtip devices that are currently in use or in a testing stage are sketched.

The concept of winglets was originally developed in the late 1800s by British aerodynamicist F.W. Lancaster, who patented the idea that a vertical surface (end plate) at the wingtip would reduce drag by controlling wingtip vortices [1]. Unfortunately, the concept never demonstrated its effectiveness, in practice because the increase in drag due to skin friction and flow separation outweighed any lift-induced drag benefit.

After the cost of jet fuel skyrocketed in the 1973 oil crisis, airlines and aircraft manufacturers explored many ways to reduce fuel consumption by improving the operating efficiency of their aircraft. R.T. Whitcomb, an engineer at NASA Langley Research Center, inspired by an article in Science Magazine on the flight characteristics of soaring birds and their use of tip feathers to control flight, continued on the quest to reduce cruise drag and improve aircraft performance and further developed the concept of winglets in the late 1970s [2]. Whitcomb, designed a winglet using advanced airfoil concepts integrated into a swept, tapered planform that would interact with the wingtip airflow to reduce drag.

Whitcomb's analysis of flow phenomena at the tip showed that the airflow about the wingtip of the typical aircraft in flight is characterized by a flow that is directed inward above the wingtip and a flow that is directed outward below the wingtip. Whitcomb hypothesized that a vertical, properly cambered and angled surface above or below the tip could utilize this cross flow tendency to reduce the strength of the trailing vortex and, thereby, reduce the lift-induced drag. In essence, Whitcomb and his team provided the fundamental knowledge and design approach required for an extremely attractive

---

* Corresponding author.
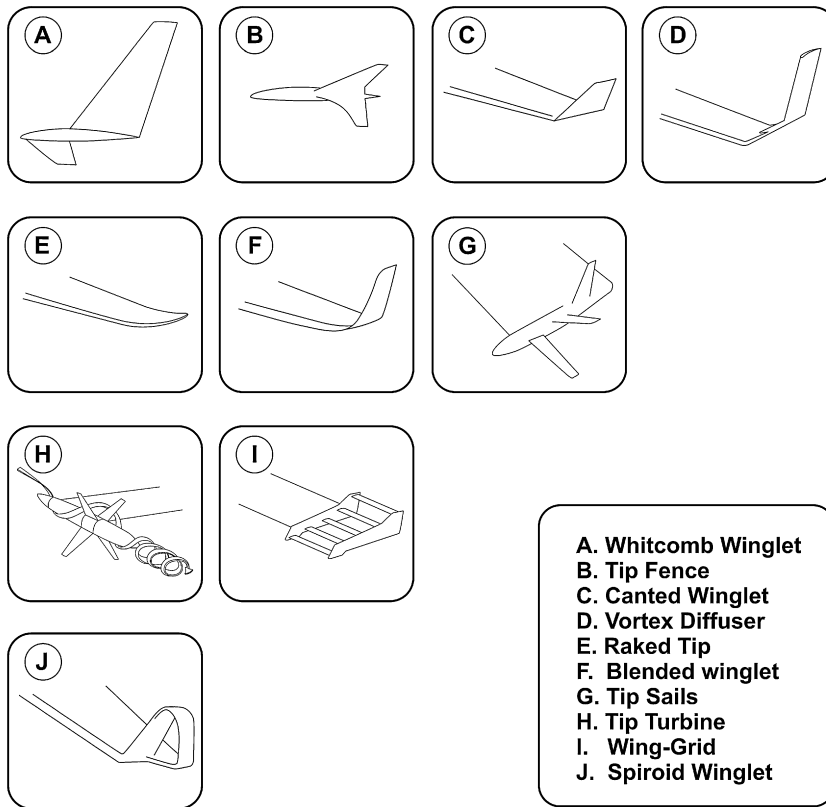 *E-mail address:* joel.guerrero@unige.it (J.E. Guerrero).

Fig. 1. Wingtip devices currently in use or in testing stage.

A. Whitcomb Winglet
B. Tip Fence
C. Canted Winglet
D. Vortex Diffuser
E. Raked Tip
F. Blended winglet
G. Tip Sails
H. Tip Turbine
I. Wing-Grid
J. Spiroid Winglet

option to improve the aerodynamic efficiency of civil and military aircraft, reducing fuel consumption and increasing operating range [2].

Besides improved fuel economy and increased range, aircraft manufacturers and winglet retrofit companies have reported that winglets also offer higher operating altitudes, improved aircraft roll rates, shorter time-to-climb rates, lower take-off speeds, less take-off noise and reduced engine emissions [3,4]. Wingtip devices for drag reduction are now standard equipment on many civil and military aircraft; however, this is a field where there is still room for improvement and innovative developments.

2. Biomimetics by abstraction: from birds' wingtip feathers to winglets on airplanes

In this manuscript we tackle the problem of lift-induced drag and tip vortices mitigation by looking at the analogous problem in nature. Birds' wingtip feathers with their large variety in morphology are biological examples to examine. In Fig. 2, it can be seen how the wingtip feathers of different birds are bent up and separated (like the fingers of a spreading hand). This wingtip feathers slotted configuration is thought to reduce the lift-induced drag caused by wingtip vortices. Tucker [5] showed for the first time that the presence or absence of these tip slots has a large effect on the drag of birds. He found that the drag of a Harris hawk gliding freely at equilibrium in a wind tunnel increased markedly when the tip slots were removed by clipping the primary feathers. The slots also appear to reduce drag by vertical vortex spreading, because the greater wingspan and other differences in the bird with intact tip slots did not entirely account for its lower drag.

Fig. 2 clearly illustrates Nature's solution for drag reduction and lift enhancement. By engineering Nature's principle behind the wingtip feathers, it is clear that tip sails [6–8], can be used as wingtip devices for drag reduction. But this implementation by biomimetics abstraction can be improved even further and aesthetically adapted to wings by designing a spiral loop, that externally wraps the tip sails (see Fig. 3). The spiroid winglet looks like an extended blended wingtip, bent upward by 360 degrees (as if rolled inboard about a longitudinal axis) to form a large rigid ribbon. L.B. Gratzer (former Boeing aerodynamics chief), who initially developed the technology [9], claims that his patented spiroid-tipped wing produces a reduction in lift-induced drag, much like that of a wing with a conventional winglet. He also claims that it highly attenuates and may even nearly eliminate concentrated wingtip vortices.

It is clear that identical copies from Nature to man-made technologies are not feasible in biomimetics. Instead, biomimetics encompasses a creative conversion into technology that is often based on various steps of abstractions and modifications,

Fig. 2. Birds' wingtip feathers. (A) Kea. (B) Pacific Brown Pelican. (C) Red Tailed Hawk. (D) Bald Eagle. (E) Northern Hawk Owl. (F) Great Blue Heron. Images courtesy of Ad Wilson (www.naturespicsonline.com) and Rob McKay (http://robmckayphotography.com).

i.e., an independent successive construction that is rather a "*new invention*" than a blueprint of Nature [10]. Our proposed solution is obtained when joining the tip of a quasi-vertical winglet extending from one half of the tip chord of the wing, with a horizontal extension from the quasi-vertical winglet extending from the other half of the wing's tip chord (see Fig. 4).

It is worth mentioning that we do not use any winglet design or optimization criteria when designing the proposed spiroid winglet. Instead, it is built in a very heuristic way, by just splitting the wingtip with two winglets and joining them with an additional horizontal segment. In order to smoothen the transition between the wing and the spiroid winglet, a small joining section is added (see Fig. 4). Then, the spiroid winglet is attached to the clean wing (shown in Fig. 5), and an extensive campaign of numerical simulations using the clean wing and the wing with the spiroid winglet is conducted. At this point, it becomes clear that if, by using this simple biomimetics approach (without any optimization or design principle involved insofar), we are able to obtain some benefit in terms of lift-induced drag reduction, wingtip vortices intensity reduction and lift enhancement, the approach proves to be worthwhile and further wingtip design and optimization deserves to be carried out.

Previous published work on similar configurations is limited to the work by Wan et al. [11] and Nazarinia et al. [12]. In Ref. [11] the effect of different winglet types (including spiroid winglets) is studied numerically focusing on wingtip vortices and aerodynamic performances, compared to a reference wing; it is found that the lift and drag coefficients are improved in all cases when winglets are adopted. Nazarinia et al. [12] conduct a parametric investigation on the effect of different winglet shapes on the flow field behind a tapered wing. They found that the total pressure in the wake is significantly influenced by the type of winglet adopted (including spiroid winglets), and so is the intensity of the vortices released at the wingtips; however, no quantitative results on lift and drag coefficients are provided.
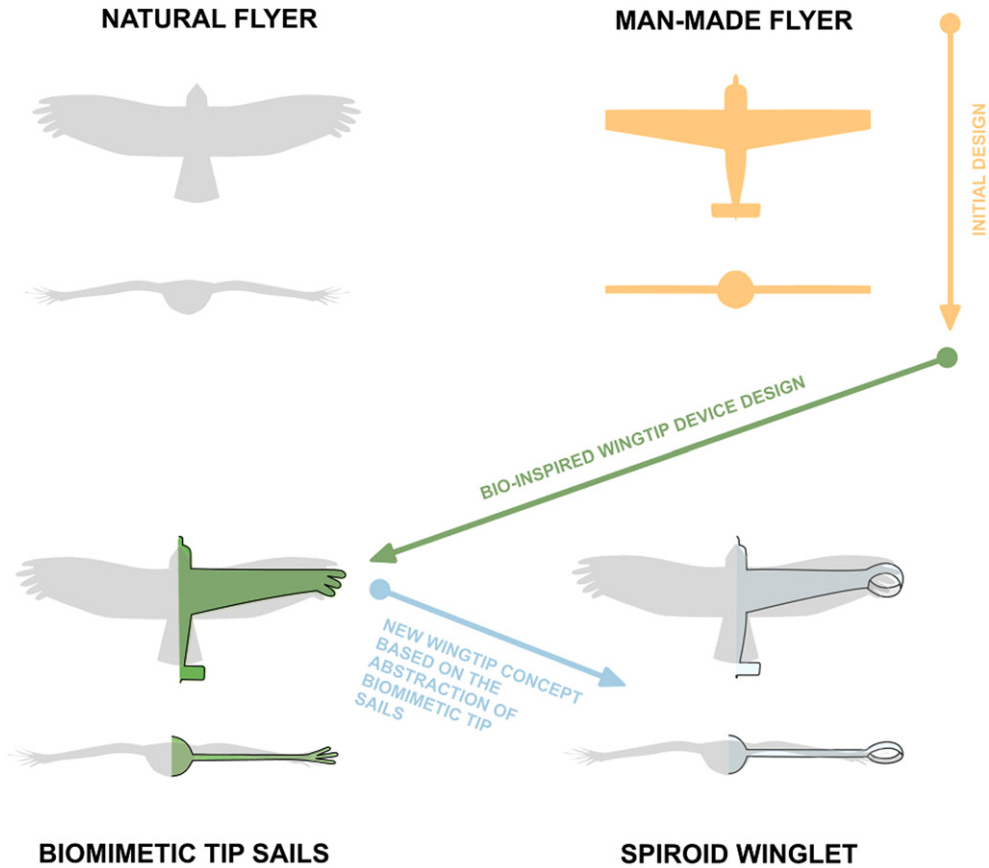
Fig. 3. Spiroid winglet design by biomimetics abstraction.

3. Lift and drag of finite span wings

Finite span wings generate lift due to the pressure imbalance between the bottom surface (high pressure) and the top surface (low pressure). However, as a byproduct of this pressure differential, cross flow components of the velocity are generated. The higher pressure air under the wing flows around the wingtips and tries to displace the lower pressure air on the top of the wing. This flow around the wingtips is sketched in Fig. 6. These structures are referred to as wingtip vortices and very high velocities and low pressure exist at their cores. These vortices induce a downward flow, known as the downwash and denoted by w, as illustrated in Fig. 6. This downwash has the effect of tilting the free-stream velocity to produce a local relative wind, which reduces the angle of attack (*AOA*) that each wing section effectively sees; moreover, it creates a component of drag, the lift-induced drag.

After having introduced the notion of lift-induced drag, we can now write the equation for the total drag of a wing as the sum of the parasite drag (which is basically the sum of the skin friction drag and pressure drag due to flow separation) and the induced drag, or in non-dimensional form:

$$C_D = C_{D0} + C_{Dind} \tag{1}$$

where C_{D0} is the drag coefficient at zero-lift and is know as the parasite drag coefficient, which is independent of the lift. The second term on the right-hand side of Eq. (1) is the lift-induced drag coefficient C_{Dind}, defined by

$$C_{Dind} = \frac{C_L{}^2}{\pi e A\!R} \tag{2}$$

In Eq. (2), C_L is the wing lift coefficient, $A\!R$ the wing aspect ratio and e is the Oswald efficiency factor (which is a correction factor that accounts for the difference between the actual wing and an ideal wing having the same aspect ratio and an elliptical lift distribution) or wingspan efficiency. Eq. (2) can be rewritten as,

$$C_{Dind} = K C_L{}^2 \tag{3}$$

where we have replaced $1/(\pi e A\!R)$ by K, a factor which clearly depends on the wing geometry. Substituting Eq. (3) in Eq. (1) we obtain,
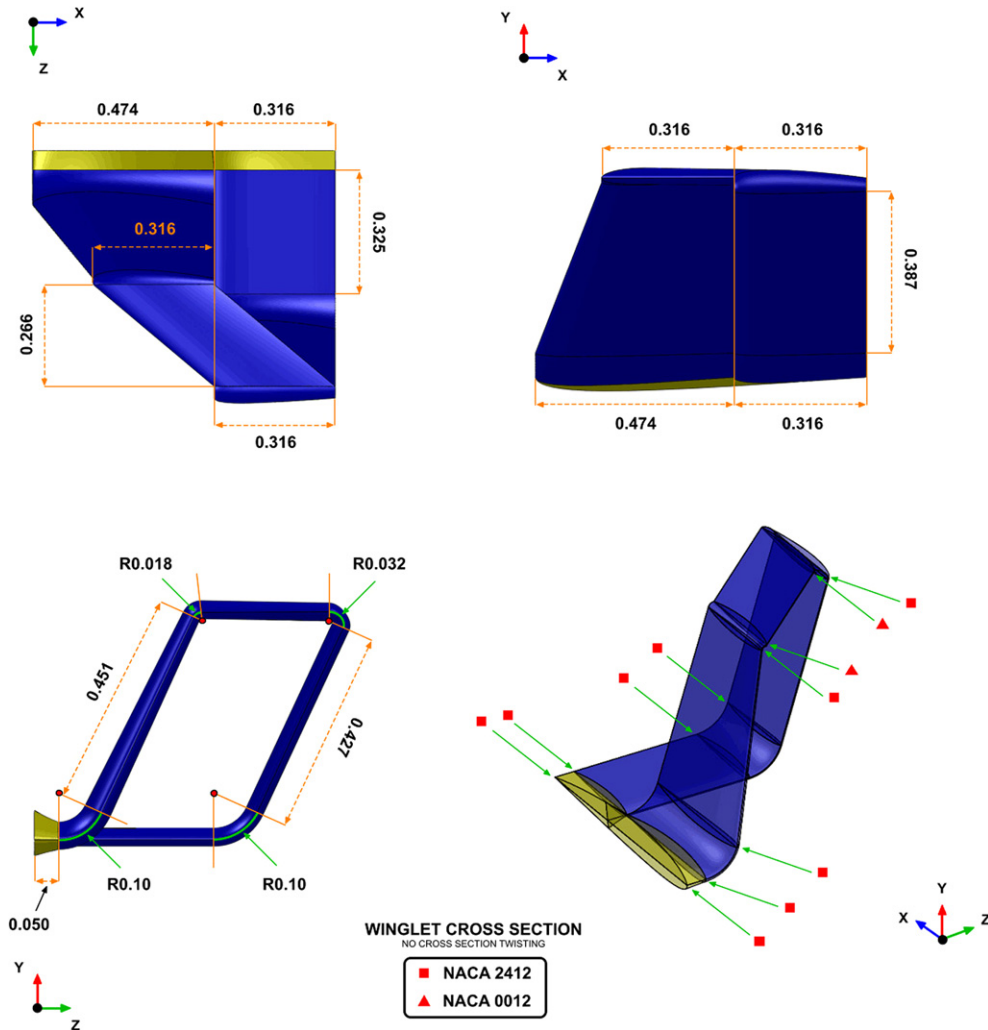
$$C_D = C_{D0} + K C_L{}^2 \tag{4}$$

Fig. 4. Spiroid winglet geometry (in blue). The joining section between the clean wing and the spiroid winglet is shown in yellow (all the dimensions are in meters).

Eq. (4) can be used to draw the drag polar of a wing with a symmetric or uncambered profile, where C_{D0} is also the minimum drag coefficient $C_{D\,\min}$, and this situation is reflected in the extremum of the parabolically shaped drag polar intersecting the horizontal axis, where C_L is equal to 0 (as sketched in Fig. 7). In this figure, the tangent line to the drag polar curve drawn from the origin of coordinates locates the point of maximum lift-to-drag ratio or $(C_L/C_D)_{\max}$. The intercept of the drag polar curve with the axis C_D is C_{D0}. The area comprised between the polar curve $C_{D0} + KC_L{}^2$ and C_{D0} is C_{Dind}. Note that each point on the drag polar corresponds to a different angle of attack of the wing.

For real wings configurations (cambered wings), when the wing is pitched to its zero-lift angle of attack $(AOA)_{L=0}$ (usually a small negative angle of attack *AOA*), C_{D0} may be slightly above the minimum drag coefficient value $C_{D\,\min}$. This situation is sketched in Fig. 8. In this figure, the drag polar curve is translated vertically a small distance with respect to that plotted in Fig. 7; the shape of the curve, however, remains the same. The new equation for the drag polar becomes

$$C_D = C_{D\,\min} + K(C_L - C_{Lmindrag})^2 \qquad (5)$$

In Eq. (5), $C_{D\,\min}$ is the minimum drag coefficient that usually occurs at some small angle of attack *AOA* slightly above $(AOA)_{L=0}$, and $C_{Lmindrag}$ is the lift coefficient at $C_{D\,\min}$. The difference between C_{D0} and $C_{D\,\min}$ is sometimes referred as to camber drag at zero-lift. This difference is usually very small and tends to be ignored. In this manuscript, we do not make this assumption and hence we represent the drag polar by using Eq. (5).

4. Numerical results and discussion

The incompressible Reynolds-Averaged Navier–Stokes (RANS) equations are numerically approximated by using the open source finite volume solver OpenFOAM [13]. The cell-centered values of the variables are interpolated at the face locations
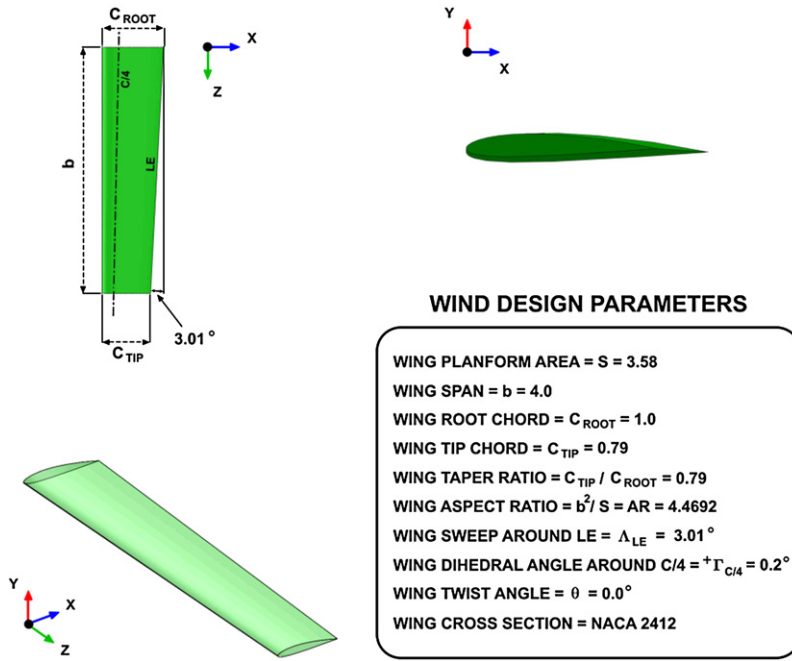
WIND DESIGN PARAMETERS

WING PLANFORM AREA = S = 3.58
WING SPAN = b = 4.0
WING ROOT CHORD = C_{ROOT} = 1.0
WING TIP CHORD = C_{TIP} = 0.79
WING TAPER RATIO = C_{TIP} / C_{ROOT} = 0.79
WING ASPECT RATIO = b^2/ S = AR = 4.4692
WING SWEEP AROUND LE = Λ_{LE} = 3.01°
WING DIHEDRAL ANGLE AROUND C/4 = $^+\Gamma_{C/4}$ = 0.2°
WING TWIST ANGLE = θ = 0.0°
WING CROSS SECTION = NACA 2412

Fig. 5. Clean wing geometry (all linear dimensions are to be intended in meters).
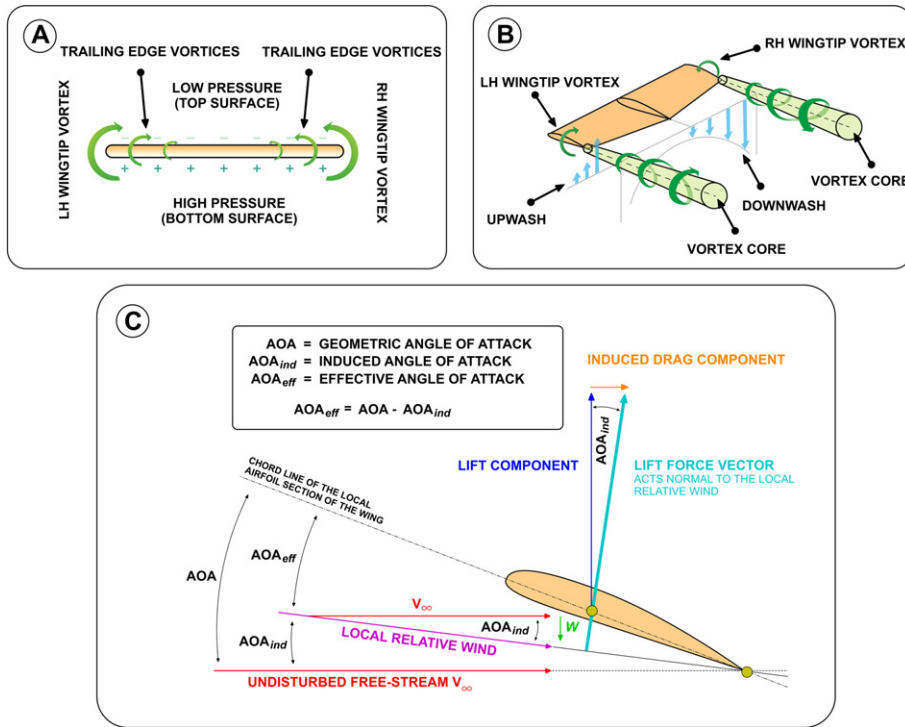
Fig. 6. (A) Illustration of lift generation due to pressure imbalance and its associated wingtip and trailing edge vortices. (B) Illustration of wingtip vortices rotation and the associated downwash and upwash. (C) Illustration of lift-induced drag generation due to downwash.

using a second-order centered difference scheme for the diffusive terms. The convective terms are discretized by means of the so-called limited linear scheme, a second-order accurate bounded total variation diminishing (TVD) scheme, resulting from the application of the Sweby limiter to the centered differencing scheme in order to enforce monotonicity [14]. The pressure-velocity coupling is achieved by means of the SIMPLE algorithm [15]. For the turbulence modeling, the Spalart–Allmaras model is used [16].
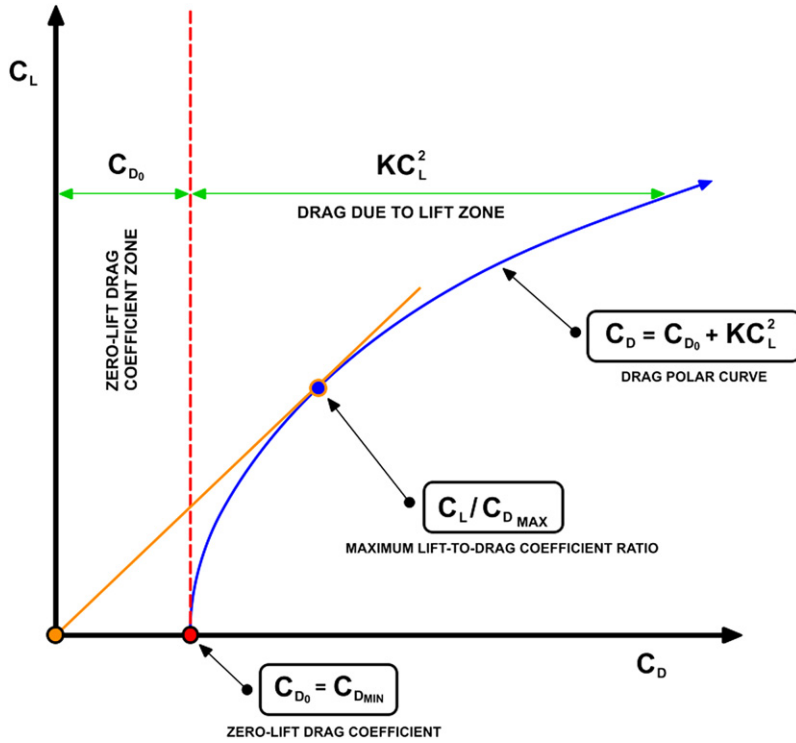
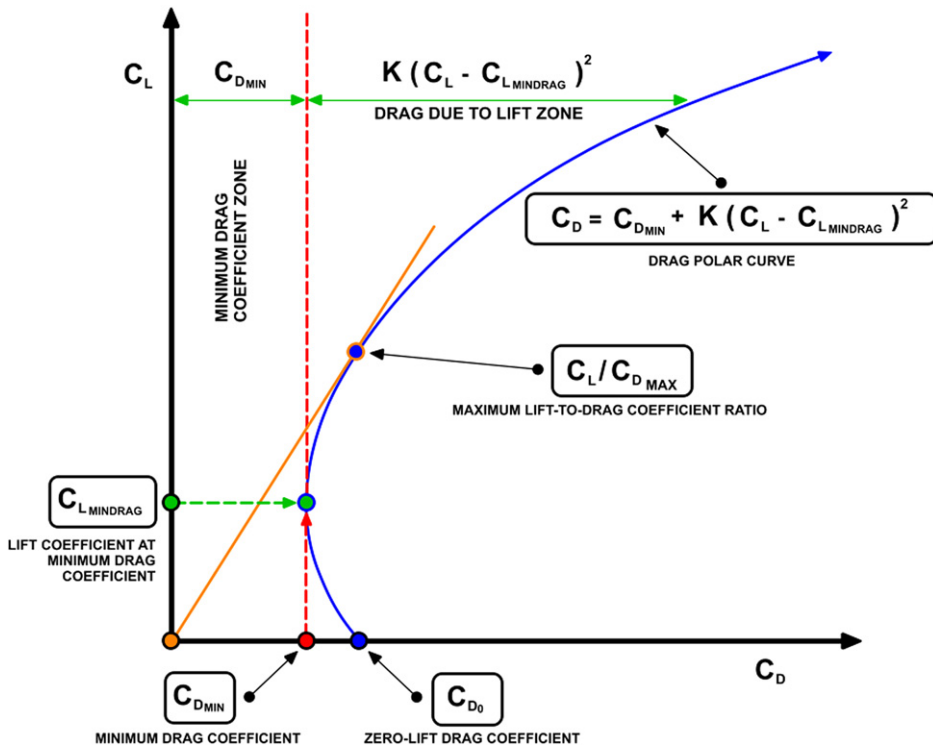**Fig. 7.** Example of a drag polar for an uncambered wing.

Fig. 8. Example of a drag polar for a cambered wing. Notice that the difference between C_{D0} and $C_{D\,min}$ has been exaggerated.
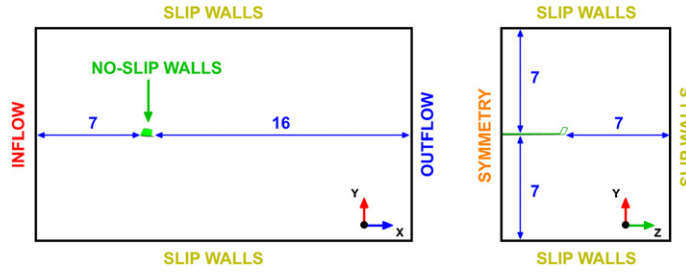
Fig. 9. Computational domain and boundary conditions (all dimensions are in meters).
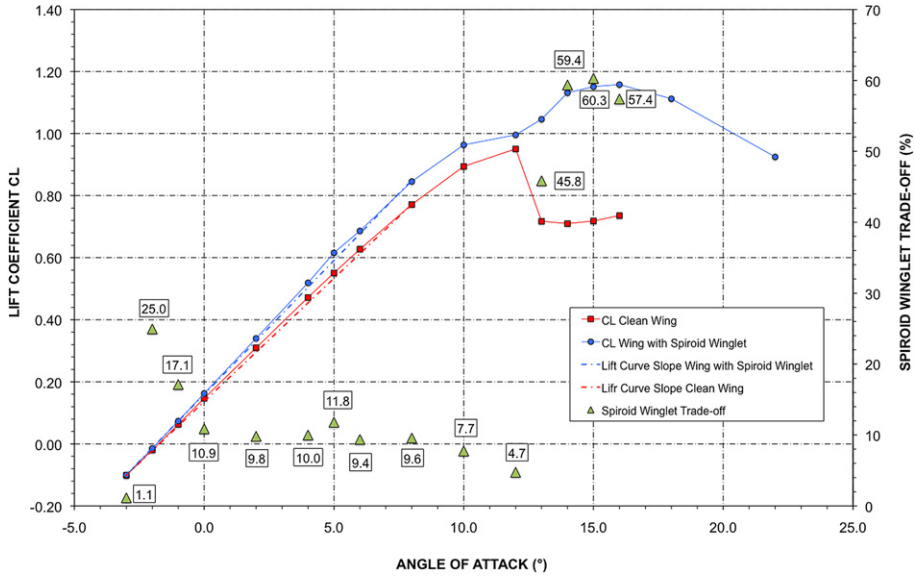

Fig. 10. Lift coefficient versus angle of attack for the clean wing (CW) and the wing with the spiroid wingtip (WSW).

An extensive campaign of simulations for the clean wing (CW) and the wing with the spiroid wingtip (WSW) has been carried out. The lift force L and drag force D are calculated by integrating the pressure and wall-shear stresses over the wing surface for each case; then, the lift coefficient C_L and drag coefficient C_D are computed as follows:

$$C_L = \frac{L}{0.5\rho V_\infty^2 S_{ref}}, \qquad C_D = \frac{D}{0.5\rho V_\infty^2 S_{ref}} \tag{6}$$

where ρ is the air density ($\rho = 1.225$ kg/m^3), V_∞ the free stream velocity (measured in m/s) and S_{ref} the wing reference area (measured in m^2). For the CW the reference area used for C_L and C_D computations is equal to 3.58 m^2 (planform area). For the WSW the reference area used for C_L computations is based on its effective span (the clean wing span plus the winglet added span) and is equal to 3.95 m^2 (approximately 10.5% larger than the reference area for the CW); for C_D computations the reference area is based on the sum of the planform area of the clean wing plus the total planform area of the spiroid winglet and is equal to 4.25 m^2 (approximately 18.75% larger than the reference area for the CW).

For all the simulations, the incoming flow is characterized by a low turbulence intensity (TU = 1.0%) and a Reynolds number $Re = \rho V_\infty L_{ref}/\mu = 100\,000$, where μ is the dynamic viscosity ($\mu = 0.000018375$ Pa s) and L_{ref} is equal to the wing's root chord ($L_{ref} = C_{root} = 1$ m). In Fig. 9, a sketch of the computational domain and the boundary conditions layout is shown. The inflow in this figure corresponds to a *Dirichlet* type boundary condition and the outflow to a *Neumann* type boundary condition. All the computations are initialized using free-stream values.

A hybrid mesh is used for all the simulations, with prismatic cells close to the wing surface and tetrahedral cells for the rest of the domain. For all of the results presented herein, the turbulence transport equations are integrated all the way to the walls, thus no wall functions are used. In all cases, the distance from the wing surface to the first cell center off the surface is less than four viscous wall units ($y^+ < 4$). A typical mesh is made-up of approximately 14 millions elements.

Computations are carried out on two 2-way quad-core Opteron 2.1 GHz CPUs, each one with 16 GB of RAM and each case takes approximately 16 hours to converge.
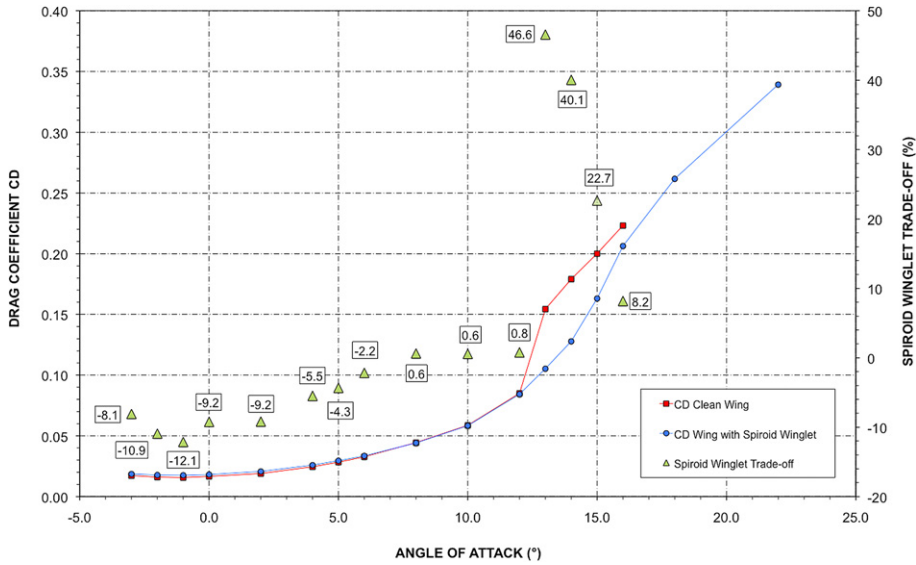
Fig. 11. Drag coefficient versus angle of attack for the clean wing (CW) and the wing with the spiroid wingtip (WSW).
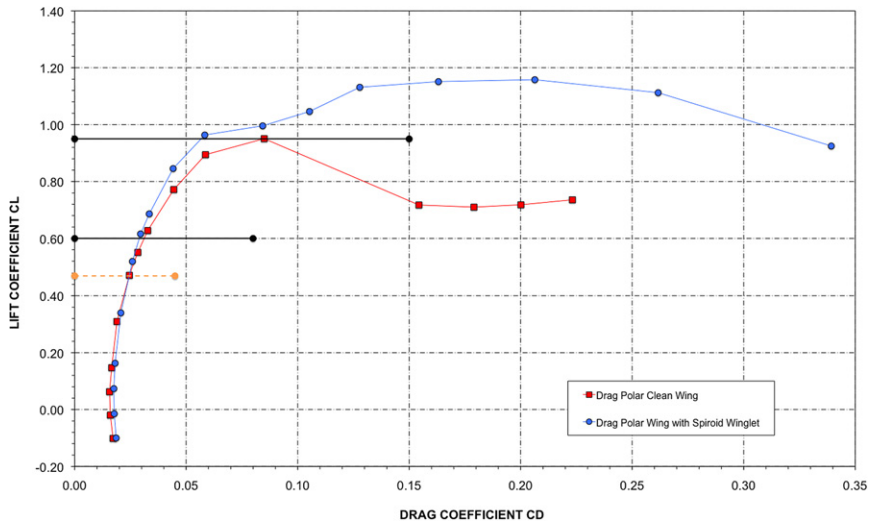

Fig. 12. Drag polars for the clean wing (CW) and the wing with the spiroid wingtip (WSW). The two horizontal black segments (with continuous lines) are drawn to show where the curves intersect $C_L = 0.95$ and $C_L = 0.60$. The horizontal orange segment (with dashed lines) is drawn to show the crossover point.

4.1. Lift coefficient

Let us first see how the lift coefficient C_L changes with the angle of attack AOA for the clean wing and the wing with the spiroid wingtip. In Fig. 10, it is observed that when the angle of attack has reached $0.0°$ there is already a definite lift coefficient and this is a property of most cambered wings. Between $AOA = -3.0°$ and $AOA = 8.0°$ the graph for both wings shows that as the angle of attack increases there is a steady linear increase in C_L. For the CW the lift curve slope is $(\partial C_L/\partial AOA) = 0.0793$ per degree and for the WSW it is $(\partial C_L/\partial AOA) = 0.0863$ per degree, which translates in approximately 9.0% increase in the lift slope between $-3.0°$ and $8.0°$. For values of angle of attack above $10.0°$, although C_L still increases for a few degrees, the increase is now comparatively small and the curves level off reaching a maximum value, the stall angle. For the CW it is found that the stall angle occurs at approximately $12.0°$, whereas for the WSW the stall angle is delayed to about $16.0°$. A clear difference can also be observed in the post-stall behavior. For the clean wing, C_L abruptly drops after the stall angle, whereas for the WSW the drop in C_L is very mild. In the same figure, the winglet trade-off or the increase in C_L with reference to the clean wing is also shown. Finally, for the CW, the angle of attack for $C_L = 0.0$ is approximately equal to $-1.75°$ and for the WSW $-1.85°$.
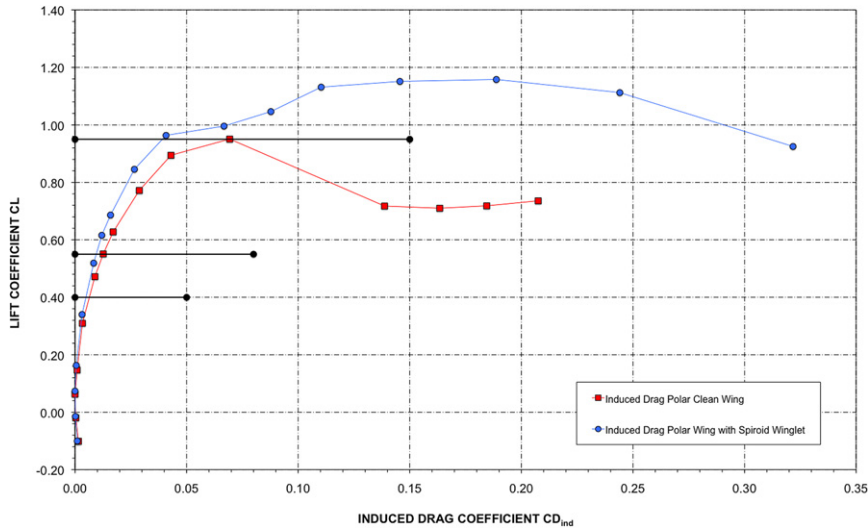
Fig. 13. Induced drag polars for the clean wing (CW) and the wing with the spiroid wingtip (WSW). The three horizontal black segments (with continuous lines) are drawn to show where the curves intersect $C_L = 0.95$, $C_L = 0.55$ and $C_L = 0.40$.
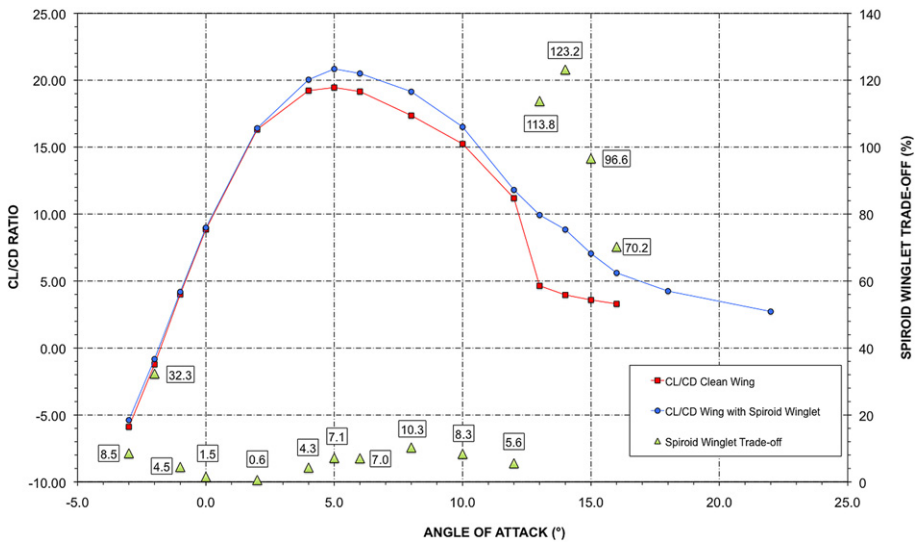

Fig. 14. C_L/C_D ratio for the clean wing (CW) and the wing with the spiroid wingtip (WSW).

4.2. Drag coefficient

The drag coefficient versus angle of attack *AOA* is shown in Fig. 11. In this figure, drag is minimum close to 0.0° and even slightly below it, and increases as we increase the angle of attack in both directions. Up to about 8.0°, however, the increase in C_D is not very rapid, then it gradually becomes more and more rapid, especially after the stalling angle. From the figure it can be seen that $C_{D\,\text{min}}$ for the CW is equal to 0.0156 at −1.0°. For the WSW, $C_{D\,\text{min}}$ is equal to 0.0175 at −1.0°. As in the case of Fig. 10, we also indicate the spiroid winglet trade-off, where negative values indicate an increase of C_D with reference to the clean wing. It is observed that there is no apparent reduction in C_D except for angles of attack above 8.0°, and basically this is due the fact that by adding the winglet we have increased the wing surface, so that skin friction is larger. Moreover, as the lift coefficient increases with the angle of attack, we expect a higher C_D value (since C_{Dind} is proportional to C_L^2). Consequently, it is difficult to determine if the WSW is superior to the CW, at least for angles of attack less than 8.0°. In order to establish the superiority (or inferiority) of the WSW it is appropriate to inspect the drag polar.
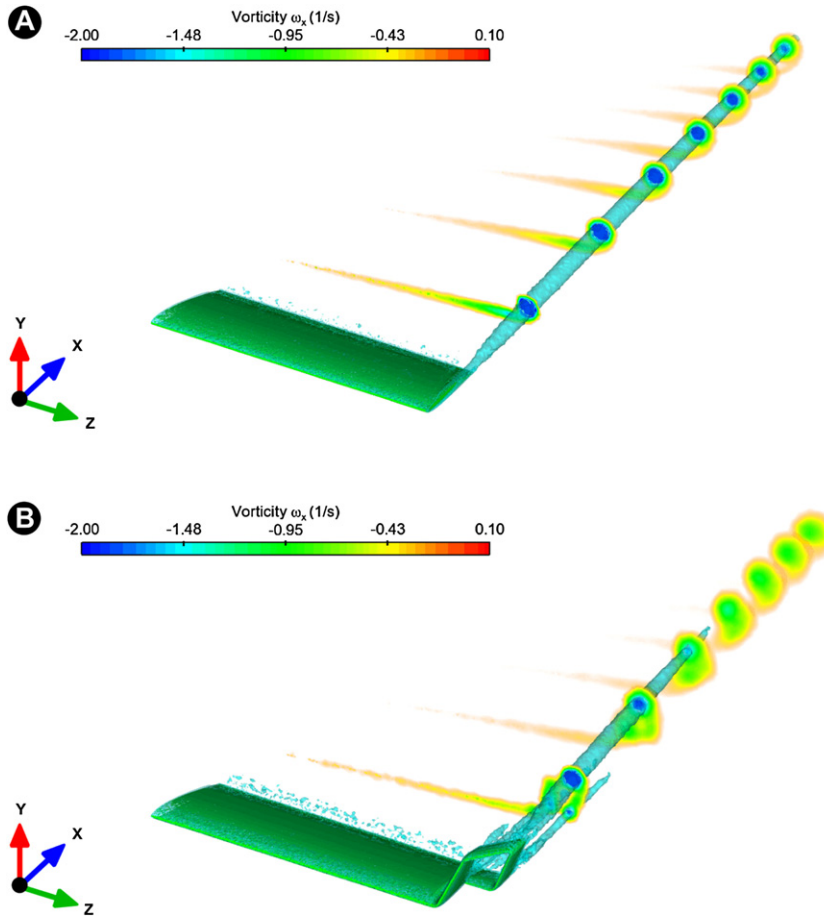
Fig. 15. Wingtip vortices (in light blue), visualization by iso-surfaces of Q-criterion ($Q = 0.5$ $1/s^2$). The equally spaced planes behind the wing are colored by vorticity ω_x. (A) Perspective view of the clean wing at $AOA = 5.0°$. (B) Perspective view of the wing with spiroid winglet at $AOA = 5.0°$.

4.3. Drag polar

In Fig. 12, we show the drag polar for both wings. From this figure, C_{D0} for the CW is approximately equal to 0.0159 ($\approx -1.50°$ AOA), and for the WSW it is approximately equal to 0.0176 ($\approx -1.30°$ AOA). The C_{D0} values reflects an increase of the parasite drag of about 10.5% for the WSW, and this is due to the added surface. Let us now establish the trade-off of the winglet by looking at the crossover point on the drag polar, or the point where the drag benefits overcome the drag penalties of the winglet. While the added length of the winglet contributes to increasing the effective span of the wing (thus reducing lift-induced contributions to drag), the increased wetted surface and the addition of the junction section increases parasite drag through additional friction and interference drag. Thus, a wing will demonstrate an overall drag reduction if it operates above the crossover point [17,18]. It is observed that for C_L values approximately lower than 0.47 ($\approx 3.50°$ AOA), the WSW for a given C_L value produces more C_D. Conversely, for values of C_L larger than 0.47, the WSW produces less C_D for a given C_L value, that is, the reductions in induced drag overcome the parasitic penalties. As an example, the overall drag reduction for the WSW is approximately 7.0% at $C_L = 0.60$ and as high as 50.0% for $C_L = 0.95$.

Additionally, in Fig. 13 we show the drag polar as function of the induced drag coefficient C_{Dind}, found by using Eq. (5). In this figure, it is clear that the WSW generates less C_{Dind} throughout the polar curve, hence the WSW is superior to the CW, at least in terms of C_{Dind} reduction. For example, the largest C_{Dind} reduction is of about 75.0% at $C_L = 0.95$; at $C_L = 0.55$ it is approximately 35.0% and at $C_L = 0.40$ the C_{Dind} reduction is close to 28.0%.

4.4. Lift-to-drag ratio

Next, we show the relation between C_L and C_D at various angles of attack (Fig. 14). It is clear that we want to generate as much lift with as little drag as possible. From the lift curve we find that we achieve most lift at about 12.0° for the CW and 16.0° for the WSW; from the drag curve we find $C_{D\,min}$ is equal to 0.0156 at $-1.0°$ for the CW, and equal to 0.0175 at $-1.0°$ for the WSW. However, the previous scenarios are at the extreme range of all the possible angles, and at neither of them we really get the best C_L/C_D ratio. It is found that the ratio C_L/C_D increases very rapidly up to about 4.0°, at
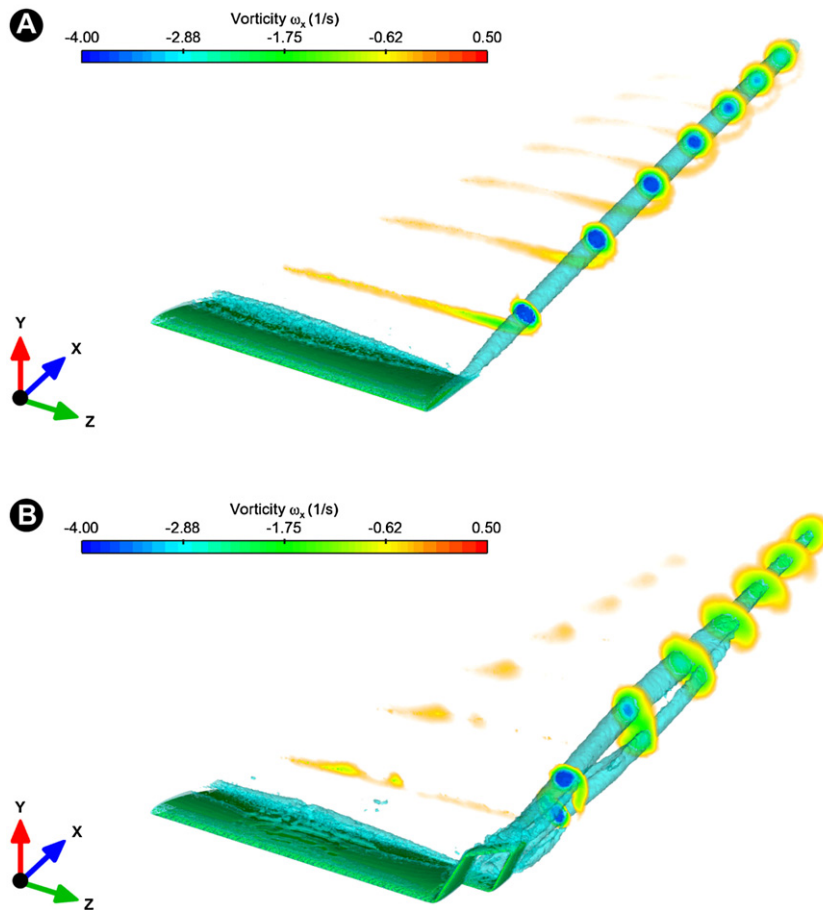
Fig. 16. Wingtip vortices (in light blue), visualization by iso-surfaces of Q-criterion ($Q = 0.5$ 1/s^2). The equally spaced planes behind the wing are colored by vorticity ω_x. (A) Perspective view of the clean wing at $AOA = 12.0°$. (B) Perspective view of the wing with spiroid winglet at $AOA = 12.0°$.

which angle C_L is nearly 19 times C_D for the CW and approximately 21 times for the WSW; then the C_L/C_D ratio gradually drops mainly because drag increases more rapidly than lift. After the stall angle, lift is approximately 5 times as large as drag for the CW and close to 8 times for the WSW. The chief point of interest about the C_L/C_D curve is the fact that this ratio is maximum at an angle of attack of about 5.0° for both wings; in other words, it is at this angle of attack that the wings give their best all-round results, *i.e.*, they will generate as much C_L as possible with a small C_D production. As for Figs. 10 and 11, we also present the spiroid winglet trade-off for this case, where positive values indicate an increase of C_L/C_D with respect to the clean wing. In the figure, the trade-off for the angle of attack equal to 5.0° ($C_L/C_{D\,\max}$) is 7.1% and the maximum trade-off value in a no-stall configuration is close to 10.0% ($AOA = 8.0°$). It can be also evidenced that close to stall and in the post-stall regime the WSW shows a less abrupt fall of C_L/C_D.

4.5. Vortex system

In this section we present a qualitative and quantitative study of the wingtip vortices, for both wings. In Figs. 15 and 16, the wingtip vortices are visualized for two different angles of attack by using the Q-criterion [19]. Additionally, the component ω_x of the vorticity is displayed at seven different planes equally spaced behind the wing, with the first plane located two meters away from the trailing edge.

As it can be seen from these figures, the WSW wingtip vortices dissipate much faster and this is observed by just looking at the wake extension, which is shorter for the WSW. Another interesting feature of the wingtip vortices for the WSW is the fact that close to the wing, the wingtip vortex is made up by two/three coherent patches of vorticity which are shed from the corners of the spiroid wingtip. The intensity of these vortices is less than the intensity of the single vortex for the CW, and as they are convected downstream, they join forming a vortex dipole, which presumably is the reason why these flow structures dissipate much faster.

In Tables 1 and 2, we present the values of the minimum pressure and maximum vorticity intensity at each plane behind the wing; the values were measured at the vortex core for the cases shown in Figs. 15 and 16. Additionally, we also show the results for the CW and WSW at $AOA = 0.0°$ and $AOA = 16.0°$. These quantitative results confirm the previous observations

Table 1

Minimum relative pressure at the vortex core (measured in Pa).

Case	Plane position						
	+2 m	+4 m	+6 m	+8 m	+10 m	+12 m	+14 m
0° CW	−0.0143	−0.0103	−0.0076	−0.0055	−0.0050	−0.0041	−0.0039
0° WSW	−0.0070	−0.0069	−0.0056	−0.0038	−0.0032	−0.0029	−0.0028
5° CW	−0.1814	−0.0994	−0.0749	−0.0601	−0.0494	−0.0421	−0.0368
5° WSW	−0.0803	−0.0413	−0.0386	−0.0276	−0.0273	−0.0238	−0.0192
12° CW	−0.5353	−0.3169	−0.2352	−0.1769	−0.1448	−0.1253	−0.1009
12° WSW	−0.1937	−0.1317	−0.0976	−0.0859	−0.0753	−0.0723	−0.0601
16° CW	−0.7467	−0.3713	−0.2620	−0.2026	−0.1598	−0.1316	−0.0999
16° WSW	−0.2225	−0.1334	−0.1140	−0.0947	−0.0853	−0.0824	−0.0630

Table 2

Maximum vorticity magnitude at the vortex core (measured in 1/s).

Case	Plane position						
	+2 m	+4 m	+6 m	+8 m	+10 m	+12 m	+14 m
0° CW	2.4544	1.3306	0.9418	0.7608	0.6432	0.5544	0.5063
0° WSW	1.6592	0.6286	0.4378	0.3890	0.3261	0.2913	0.2713
5° CW	8.6725	4.9520	3.6494	2.8121	2.3942	2.1426	1.8370
5° WSW	5.0927	2.1326	1.6164	1.2324	1.0731	0.9758	0.8629
12° CW	14.2090	8.6632	6.0790	4.7115	3.9445	3.3474	2.8698
12° WSW	7.1662	3.6044	2.6365	2.0501	1.8438	1.7126	1.5787
16° CW	15.6370	9.0200	6.4242	4.7728	3.7889	3.0992	2.6222
16° WSW	6.9692	3.5913	2.5138	2.0213	1.7265	1.6673	1.4819

on the lower intensity of the wingtip vortices for the WSW and their rapid dissipation. This can be extremely beneficial for air traffic flow management at major airports, as it would reduce the aircraft spacing in terms of time and distance during landing and take-off operations, thus contributing to alleviate air traffic congestion at major hubs. A hypothetical aircraft equipped with spiroid winglets would allow the following aircraft to be spaced closer, thereby improving airports operations efficiency.

5. Conclusions

In the aeronautical field, reducing drag constitutes a challenge. The drag breakdown of a typical transport aircraft shows that the lift-induced drag can make-up as much as 40% of the total drag at cruise conditions and 80–90% of the total drag in the take-off configuration. The classical way to decrease the lift-induced drag is to increase the aspect ratio of the wing. However, wing aspect ratio is a compromise between aerodynamic performance, weight constraints, structural requirements and operational factors. The alternative is to use wingtip devices that aim at reducing the strength of the wingtip vortices, lowering the lift-induced drag.

In this manuscript, we have tested a spiroid wingtip, by adapting it to a clean wing. The performance of the wing with the spiroid winglet relative to the clean wing has been studied quantitatively and qualitatively, and the following benefits/shortcomings have been found:

Benefits:

- Lift-induced drag reduction. As much as 75.0% at $C_L = 0.95$, 35.0% at $C_L = 0.55$ and 28.0% at $C_L = 0.40$;
- Lift production enhancement. C_L is higher for the whole lift curve and its slope is increased by approximately 9.0%;
- Total drag reduction for C_L values above the crossover point $C_L \approx 0.47$. As much as 50.0% at $C_L = 0.95$, 20.0% at $C_L = 0.90$ and 7.0% at $C_L = 0.60$;
- Lift-to-drag ratio enhancement. The trade-off at $(C_L/C_D)_{\max}$ is nearly 7.1% and the maximum trade-off value in no-stall configuration is close to 10.0% ($AOA = 8.0°$);
- Wing stall delay;
- Better post-stall behavior.

Shortcomings:

- Increased parasite drag due to the increased wetted surface;
- Higher parasite drag due to interference drag in the wing junction with the winglet and in the corners of the spiroid loop;
- Increased weight due to the device itself;
- The increased static loads will require a new structural study in order to support the higher bending moments and to meet the new flutter and fatigue requirements.

Aside from the points raised above, a side benefit of the spiroid winglet used in this study is its ability to greatly reduce the intensity of the wingtip vortices, which dissipate very fast. This can be extremely beneficial for air traffic flow management at major airports, as it would reduce the aircraft spacing necessary to allow for wake vortex dissipation during landing and take-off operations.

From an airplane manufacturer or operator point of view, the benefits outlined could translate into:

- Increased operating range;
- Improved take-off performance;
- Higher operating altitudes;
- Improved aircraft roll rates;
- Shorter time-to-climb rates;
- Less take-off noise;
- Increased cruise speed;
- Reduced engine emissions;
- Meet runaway and gate clearance with minimal added span and height;
- Reduced separation distances and improved safety during take-off and landing operations due to wake vortex turbulence reduction.

It is clear that in order to achieve all of the previous assets and obtain the best trade-off between benefits and short-comings, shape optimization studies of the spiroid winglet are required.

Acknowledgements

References

[1] J. Jupp, Wing aerodynamics and the science of compromise, Aeronautical Journal 105 (1053) (November 2001) 633–641.
[2] J.R. Chambers, Concept to reality: Contributions of the Langley Research Center to U.S. Civil Aircraft of the 1990s, NASA History Series, NASA SP-2003-4529, 2003.
[3] Assessment of Wingtip Modifications to Increase the Fuel Efficiency of Air Force Aircraft, Committee on Assessment of Aircraft Winglets for Large Aircraft Fuel Efficiency, Air Force Studies Board Division on Engineering and Physical Sciences, The National Academies Press, 2007.
[4] R. Faye, R. Laprete, M. Winter, Blended winglets, M. Aero, No. 17, Boeing, January 2002.
[5] V.A. Tucker, Drag reduction by wing tip slots in a gliding Harris Hawk, Parabuteo Unicinctus, J. Exp. Biol. 198 (1995) 775–781.
[6] A. Hossain, A. Rahman, A. Iqbal, M. Ariffin, M. Mazian, Drag analysis of an aircraft wing model with and without bird feather like winglet, Int. J. Aeros. Mech. Eng. 6 (1) (2012) 8–13.
[7] J. Spillman, The use of wing tip sails to reduce vortex drag, Aeronaut. J. 82 (1978) 387–395.
[8] D.S. Miklosovic, Analytic and experimental investigation of dihedral configurations of three-winglet planforms, J. Fluids Eng. 130 (7) (July 2008) 0711103/1–0711103/10.
[9] L.B. Gratzer, Spiroid-tipped wing, U.S. Patent 5,102,068, 7 April 1992.
[10] I.C. Gebeshuber, M. Drack, An attempt to reveal synergies between biology and mechanical engineering, Proc. Inst. Mech. Eng. C J. Mech. Eng. 222 (7) (2008) 1281–1287.
[11] T. Wan, H.-C. Chou, K.-W. Lien, Aerodynamic efficiency study of modern spiroid winglets, in: 25th Congress of International Council of the Aeronautical, Sciences, September 2006, Germany, Paper ICAS 2006-3.7S.
[12] M. Nazarinia, M.R. Soltani, K. Ghorbanian, Experimental study of vortex shapes behind a wing equipped with different winglets, Journal of Aerospace Science and Technology 3 (1) (2006) 1–15.
[13] OpenFOAM User Guide, OpenCFD Limited. Version 2.0.0, June 2011.
[14] P.K. Sweby, High resolution schemes using flux limiters for hyperbolic conservation laws, SIAM J. Numer. Anal. 21 (1984) 995–1011.
[15] J.H. Ferziger, M. Peric, Computational Methods for Fluid Dynamics, third edition, Springer-Verlag, Berlin, 2001.
[16] P.R. Spalart, S.R. Allmaras, A one-equation turbulence model for aerodynamic flows, AIAA Paper 92-0439-CP, 1992.
[17] R.T. Whitcomb, A design approach and selected wind-tunnel results at high subsonic speeds for wing-tip mounted winglets, NASA Technical Note, NASA TN D-8260, July 1976.
[18] M.D. Maughmer, The design of winglets for high-performance sailplanes, AIAA Paper 2001-2406-CP, 2001.
[19] R. Haines, D. Kenwright, On the velocity gradient tensor and fluid feature extraction, AIAA Paper 1999-3288-CP, 1999.